

Highly efficient hot electron harvesting from graphene before electron-hole thermalization

Yuzhong Chen¹, Yujie Li¹, Yida Zhao¹, Hongzhi Zhou¹, Haiming Zhu^{1,2*}

Although the unique hot carrier characteristics in graphene suggest a new paradigm for hot carrier–based energy harvesting, the reported efficiencies with conventional photothermoelectric and photothermionic emission pathways are quite low because of inevitable hot carrier thermalization and cooling loss. Here, we proposed and demonstrated the possibility of efficiently extracting hot electrons from graphene after carrier intraband scattering but before electron-hole interband thermalization, a new regime that has never been reached before. Using various layered semiconductors as model electron-accepting components, we generally observe ultrafast injection of energetic hot electrons from graphene over a very broad photon energy range (visible to mid-infrared). The injection quantum yield reaches as high as ~50%, depending on excitation energy but remarkably, not on fluence, in notable contrast with conventional pathways with nonlinear behavior. Hot electron harvesting in this regime prevails over energy and carrier loss and closely resembles the concept of hot carrier solar cell.

INTRODUCTION

The bandgap (E_g) character of conventional semiconductor materials enables their applications in light-harvesting and optoelectronic devices, but at the same time, sets the fundamental limit of the spectral response and power conversion efficiency. For instance, the energy below E_g is not captured and any excess energy exceeding E_g is lost irreversibly to lattice as heat, leading to, e.g., Shockley-Queisser limit for photovoltaic cells (1). One way to overcome this limit and achieve far higher efficiency is extracting all energies from photoexcited carriers while they are still hot (2). This can be realized in semiconductors where scattering among photoexcited electrons is faster than electron cooling and recombination, coupled with equally fast carrier extraction by an energy selective contact.

Among potential candidate materials including semiconductor (3) and metallic (4) nanostructures and thin films, graphene with atomic layer thickness has been proposed as a promising system to explore hot carrier–assisted energy harvesting (5). Because of its unique linear band structure, graphene exhibits uniform (~2.3%) spectral response spanning infrared (IR) to visible regions (Fig. 1, i) (6, 7) and more importantly, very rapid electron-electron scattering assisted by strong Coulomb interactions (5, 8–10). Although very early stage carrier dynamics in graphene have not been explicitly resolved and analyzed, more experimental studies including ultrafast spectroscopic dynamics (8, 9, 11–13), broadband photoluminescence (PL) (14, 15), and stimulated emission in graphene (16, 17) have suggested that in the first ~10 fs, the initial photoexcited electron and hole assemblies quickly evolve into two separate hot Fermi-Dirac (FD) distributions (“quasi-thermalization”) with distinct chemical potentials ($\mu_{e(h)}^*$) and temperatures ($T_{e(h)}^*$) in conduction and valance bands, respectively, through intraband electron-electron scattering (Fig. 1, ii). Following that, there is consensus in literature that electron-hole coalescence into a single hot FD distribution (“full thermalization”) with one temperature (T_e) and chemical potential (μ , $\mu = 0$ for charge neutral graphene) in 100 to 150 fs through interband electron

scattering (including Auger and inverse Auger processes; Fig. 1, iii) and strongly coupled optical phonon emission (Fig. 1, iv) (5, 8, 10–13, 18). The thermalized hot carrier cools down slowly by further dissipating energy to phonons in picoseconds (directly or assisted by supercollision). Because of small electron heat capacity and vanishing density of states near the Dirac point, hot electrons in graphene can reach a high temperature (a few thousand Kelvin) and stay hot over a long time (up to tens of picoseconds).

Many efforts have exploited hot carrier–assisted energy harvesting in graphene, with most based on the photothermoelectric effect with in-plane junction devices (19–24). Unfortunately, these devices typically show limited photoactive areas, low quantum efficiency (~1%), and sublinear photoresponse on illumination power, limited by the operation principle and a small Seebeck coefficient of graphene. On the other hand, graphene-semiconductor

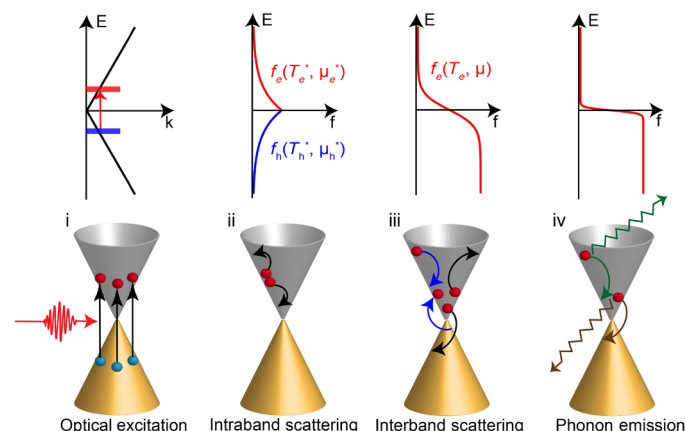


Fig. 1. Photoexcitation dynamics and corresponding carrier distributions in graphene. (i) Interband optical excitation leads to nonthermal electron-hole distribution. (ii) Electrons and holes each evolve into separate quasi-thermalized hot FD distributions with distinct temperatures ($T_{e(h)}^*$) and chemical potentials ($\mu_{e(h)}^*$) in ~10 fs, mostly through electron-electron intraband scattering. (iii and iv) Interband scattering across the Dirac point and optical phonon emission establish hot thermalized electron distribution with one temperature (T_e) and chemical potential (μ) in ~100 fs, which cools down further through emission of optical and acoustic phonons in picoseconds.

¹Center for Chemistry of High-Performance & Novel Materials, Department of Chemistry, Zhejiang University, Hangzhou, Zhejiang 310027, China. ²State Key Laboratory of Modern Optical Instrumentation, Zhejiang University, Hangzhou, Zhejiang 310027, China.

*Corresponding author. Email: hmzhu@zju.edu.cn

vertical heterostructures where the entire graphene is exposed as a photoactive region and vertical charge transfer (CT) is enabled have attracted increasing interest (25–31). An initial study on a graphene- WSe_2 -graphene heterostructure with chemical vapor deposition graphene shows sub-bandgap photocurrent generation with superlinear dependence on excitation power (26). Hot thermalized electron in graphene has a long tail toward higher energy, and the portion above a potential barrier can transfer into a semiconductor through thermionic emission, denoted as conventional one- μ photothermionic emission (1 μ PTE) pathway. However, the quantum efficiency was rather low (~2%) as a substantial amount of energy and carrier loss has occurred during thermalization (5, 10, 18), as well as subsequent electron injection, which is in competition with hot electron cooling (26). A very recent study on WS_2 -graphene heterostructure exhibits photocarrier generation in WS_2 after sub-bandgap excitation (27). The authors referred to direct interlayer CT transition to explain observed photocarrier generation (27). However, the interlayer CT transition is usually too weak (compared to intralayer transition) to serve as an efficient pathway. Given that energies and carriers are mostly stored and conserved in the initial intraband scattering process (5, 9, 10, 18), an ideal energy-harvesting strategy would be efficiently extracting quasi-thermalized hot carriers before electron-hole coalescence sets in, denoted as two- μ photothermionic emission (2 μ PTE) pathway.

We proposed and experimentally demonstrated the 2 μ PTE pathway for highly efficient hot electron harvesting from graphene to various transition metal dichalcogenides (TMDs, including MoS_2 , MoSe_2 , WS_2 , and WSe_2) as model electron-accepting components. Using ultrafast spectroscopy, we observed highly efficient upconverted hot carrier-assisted photocarrier generation in TMD layers over a broad excitation wavelength (visible to mid-IR) (Fig. 2A). Our measurement shows ultrafast (~25 fs) electron injection from graphene to TMDs under sub-bandgap excitation with quantum yield (QY) as high as ~50%. QY shows strong dependence on photon energy but remains nearly constant with varying photon density, in good agreement with the 2 μ PTE but not conventional 1 μ PTE pathway. The temperature- and gating-dependent studies further support this new pathway.

RESULTS

We fabricated graphene/TMD (MoS_2 , WS_2 , MoSe_2 , and WSe_2) heterostructure samples on SiO_2 by mechanical exfoliation and van der Waals stacking (see experimental details). The heterointerface was kept away from any polymer contamination during fabrication, and the samples were annealed under high vacuum. We kept the graphene layer on top for all samples to eliminate potential substrate effects on graphene. Figure 2B shows an optical image of a representative monolayer graphene/ WS_2 (Gr/ WS_2) heterostructure. The atomic force microscopy height profile (Fig. 2C) shows a small height difference of approximately 0.4 nm between graphene and WS_2 , suggesting a well-coupled interface (27, 32). We draw the energy level diagram (Fig. 2D) based on the 1.4-eV offset between the graphene Dirac point and the WS_2 valance band maximum from angle-resolved photoemission spectroscopy measurement (33) and a quasi-particle bandgap (~2.3 eV) of WS_2 (34, 35) without considering excitonic effect or interfacial effect. The estimated energy barrier (ϕ_B) between WS_2 conduction band minimum (CBM) and the graphene Dirac point is thus ~0.9 eV and will be ~0.2 eV smaller if we consider interlayer exciton binding energy (35–37).

We characterized the sample using reflectance contrast (δR) (Fig. 2E) and PL (fig. S9) spectroscopy. Reflectance contrast is cal-

culated as $\delta R = (I_s^R - I_0^R)/I_0^R$, where I_s^R and I_0^R are the reflected light intensity from sample and substrate (SiO_2), respectively. For atomically thin samples on a transparent SiO_2 substrate, δR directly reflects the absorption property (6). Monolayer WS_2 exhibits a sharp A exciton peak at 2 eV, which is significantly broadened and red-shifted in the Gr/ WS_2 heterostructure. This, together with orders of magnitude quenched WS_2 PL, suggests strong electronic coupling and ultrafast interfacial CT in the heterostructure (32, 38). It is worth noting that the small trion feature on WS_2 PL disappeared in heterostructures, suggesting a slight static electron flow from WS_2 to graphene (38). We determined graphene in the heterostructure to be weakly p-doped with a doped carrier concentration of $\sim 1 \times 10^{12} \text{ cm}^{-2}$ and a chemical potential of ~0.13 eV below the Dirac point from Raman spectroscopy (section S1). We compared a summed δR spectra (gray dashed line) of isolated graphene and WS_2 monolayers to that of the Gr/ WS_2 heterostructure (Fig. 2E). As was shown previously, they overlap well below WS_2 absorption (lower than 1.8 eV) (38), indicating most graphene direct interband transition with little (<5%) CT transition contribution in the Gr/ WS_2 heterostructure.

We investigated the photocarrier generation in graphene/TMD heterostructures using ultrafast transient reflectance (TR) spectroscopy (see experimental details in section S1). We pumped the heterostructures with photon energies below the TMD bandgap to excite graphene only and probed the electron population in TMD through a white light continuum. For the Gr/ WS_2 heterostructure, we chose excitation energies of 1.6 eV (775 nm), 1.37 eV (900 nm), 1.2 eV (1.03 μm), 0.95 eV (1.3 μm), 0.83 eV (1.5 μm), 0.73 eV (1.7 μm), 0.62 eV (2.0 μm), 0.52 eV (2.4 μm), and 0.36 eV (3.5 μm). Under sub-bandgap excitation, hot electron distribution has a long tail toward higher energy from electron-electron scattering and only upconverted energetic electrons above the barrier can transfer to WS_2 . The color plot of TR spectra of Gr/ WS_2 at 1.6-eV excitation (pulse duration of ~30 fs) is shown in Fig. 3A. Upon photoexcitation, TR spectra show a dominant bleach peak at ~1.98 eV, corresponding to A exciton peak of WS_2 . We observed no TR signal on an isolated WS_2 monolayer under the same condition. The WS_2 A exciton bleach under sub-bandgap excitation can only be attributed to carrier-induced broadening and band-filling effect, indicating carrier injection from photoexcited graphene to WS_2 (39). Selective carrier extraction from the Gr/ WS_2 heterostructure (section S2) confirms electron (not hole) injection to WS_2 , which is consistent with the energy level alignment and previous photocurrent measurements (26). In a small signal regime (< 0.01), the TR signal is linearly proportional to carrier population; thus, TR kinetics directly yields the electron transfer kinetics (section S4).

The TR kinetics of WS_2 A exciton bleach is shown in Fig. 3B. Fitting the kinetics yields a rising time of 27 ± 4 fs and a biexponential decay with a half-life time of ~1.2 ps, which corresponds to hot electron transfer from graphene to WS_2 and subsequent back electron transfer to graphene, respectively. Previous studies on graphene-TMD van der Waals heterostructures also reported an ultrafast interfacial process, mostly limited by experimental time resolution (27, 36, 40). This interfacial electron transfer time is orders of magnitude faster than the value (~40 ps) inferred from photocurrent measurement (26). This time scale is comparable with graphene intraband electron scattering time, which is a prerequisite for efficient hot carrier harvesting.

Key insights into the hot electron transfer process comes from examining how the TR signal peak amplitude (TR_{max}) changes with photon energy ($\hbar\nu$) and absorbed photon density (N_{photon}). We

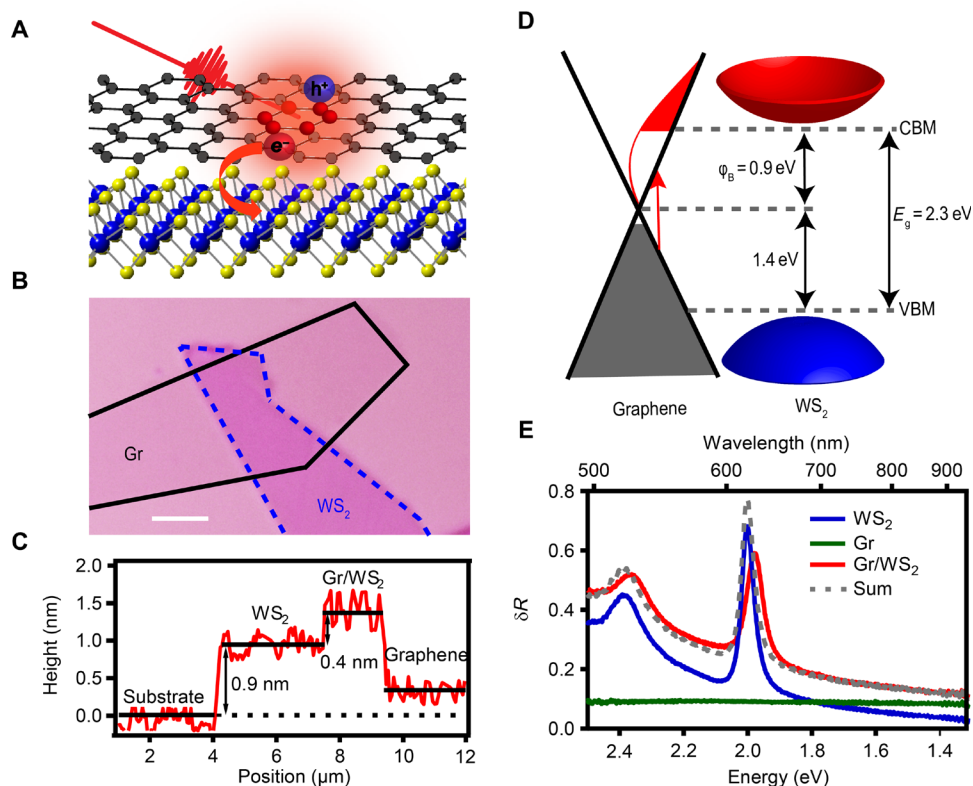


Fig. 2. Scheme and characterization of Gr/WS₂ heterostructure. (A) Scheme showing photoexcited hot electron transfer from graphene to WS₂ underneath before electron-hole coalescence. (B) Optical image of a representative Gr/WS₂ heterostructure. Scale bar, 5 μm. (C) Atomic force microscopy height profile of a Gr/WS₂ heterostructure showing a ~0.9-nm height difference between WS₂ and substrate and ~0.4 nm between graphene and WS₂. (D) Scheme of quasi-particle band alignment between graphene and WS₂. The barrier height between the graphene Dirac point and WS₂ CBM is estimated to be ~0.9 eV without considering excitonic effect or interfacial effect. VBM, valence band maximum. (E) Reflectance contrast (δR) spectra of graphene, WS₂ monolayers, and Gr/WS₂ heterostructure. The summed spectrum of isolated graphene and WS₂ monolayers is also shown for comparison, showing little contribution from interlayer CT transition.

varied $\hbar\nu$ over a wide range while always maintaining the TR signal in a small signal regime, and we observed photoelectron generation in WS₂ for all excitation conditions (fig. S10). We first analyzed the dependence of the TR_{\max} and injected electron population on N_{photon} , as shown in Fig. 3C. N_{photon} was calculated with precise pump/probe beam profiles and absorption properties (section S5). We assumed constant absorption (2.3%) from graphene in the investigated range (6, 7). Unexpectedly, TR_{\max} increases linearly with N_{photon} for all $\hbar\nu$ applied, except the onset of sublinear deviation with low-energy photons at high N_{photon} . This linear power dependence precludes multiphoton processes and indicates constant hot electron injection QY from photoexcited graphene, in notable contrast with conventional photothermionic (26, 28) and photothermoelectric graphene devices (19, 22–24), which show superlinear and sublinear power dependence, respectively. Similar linear behavior has been observed and ascribed to direct CT transition (27). CT transition cannot occur below ~0.9 eV as the band alignment sets a cutoff. CT could contribute to photocarrier generation for photon energy above 0.9 eV, but we expect this contribution to be small (<5%) on the basis of the absorption spectra. As we will show later, this linear power dependence can be well described by the proposed 2 μ PTE model but not the conventional photothermionic model.

Increasing $\hbar\nu$ leads to a larger TR signal, which can be clearly seen from the slope of linear power dependence. We determined the QY of hot electron injection from graphene, which is the figure

of merit for most applications (see section S4 for details), and the results are shown in Fig. 3D for the Gr/WS₂ heterostructure. We note that the error bars are calculated from completely different sets of measurements on the same sample. The way we determined QY sets the upper bound and has a relative uncertainty of 10% (section S3). QY exhibits a strong dependence on $\hbar\nu$, increasing monotonically from ~1% for the lowest $\hbar\nu$ (0.36 eV) to as high as ~55% for 1.6-eV excitation (~0.4 eV below the WS₂ bandgap), highlighting the importance of $\hbar\nu$ on hot electron extraction yield. The hot electron extraction yield here is significantly higher than the internal QY in previously reported graphene hot carrier-based devices (22, 26, 28). We performed the same measurements on another Gr/WS₂ sample and obtained similar results (fig. S11).

Under sub-bandgap photon excitation, only electrons with enough energy gained from an electron scattering process (“energetic electrons”) can overcome the interfacial barrier ϕ_B and inject into a semiconductor conduction band (“photothermionic emission”). In the conversational photothermionic emission (1 μ PTE) pathway (26), photoexcitation heats up carriers on graphene and creates a thermalized hot carrier distribution for the whole electronic system

$$f_e(\epsilon) = \frac{1}{\exp\left(\frac{\epsilon - \mu}{k_B T_e}\right) + 1} \quad (1)$$

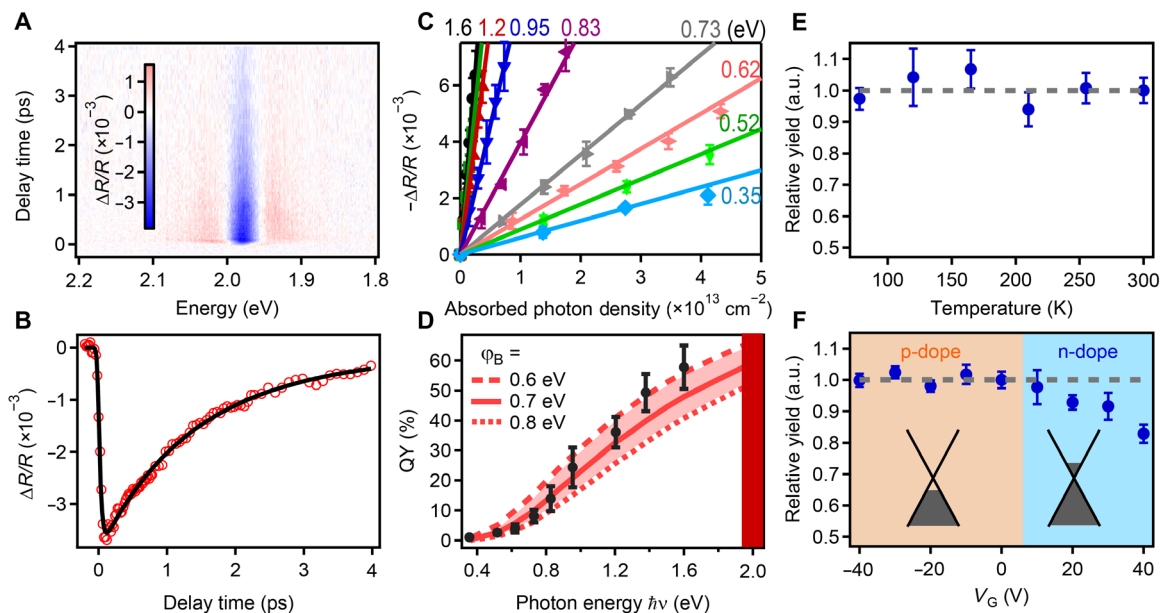


Fig. 3. Hot electron transfer from photoexcited graphene to WS₂ monolayer. (A) Color plot of TR spectra of Gr/WS₂ heterostructure under 1.6-eV excitation, clearly showing the A exciton bleach of WS₂ under sub-bandgap excitation. (B) TR kinetic at WS₂ A exciton bleach in Gr/WS₂ heterostructure showing ~25-fs rising and a ~1.2-ps decay process, corresponding to a hot electron transfer from graphene to WS₂ and a subsequent back electron transfer process. The black line is the exponential fit. (C) Peak amplitude of TR signal for different photon energies as a function of absorbed photon density, showing a clear linear dependence. Higher photon energy leads to larger peak amplitude due to hotter carrier distribution. (D) Experimentally determined QY (black circles) of hot electron transfer as a function of photon energies showing continuous increase with photon energy. Lines are predicted QY based on 2 μ PTE with different barrier heights (0.6, 0.7, and 0.8 eV). Relative hot electron injection yield ($\hbar\nu = 1.6$ eV and $N_{\text{photon}} = 4 \times 10^{12}$ cm⁻²) as a function of (E) sample temperatures (78 to 298 K) and (F) back-gating voltages (-40 to 40 V). The hot electron injection process shows negligible dependence on sample temperature. The electron inject yield is not affected by hole (p) doping but decreases with increasing electron (n) doping. a.u., arbitrary units.

with one well-defined T_e and unaltered μ . The hot electron distribution extends to high energy, and the fraction of electrons above φ_B contribute to photocurrent via thermionic emission (26, 28). We calculated hot electron distribution and injection QY at different $\hbar\nu$ (0.35 to 1.6 eV) and N_{photon} (10^{11} to 10^{13} cm⁻²) values using the 1 μ PTE model for charge-neutral graphene (see section S5 for details). As substantial energy (~30%) (26, 41) loss has occurred during the initial thermalization process, for simplicity, we assume that 70% of photon energy go to the electronic system in the 1 μ PTE model. This percentage does not affect the predicted trend.

The calculated T_e as a function of $\hbar\nu$ and N_{photon} is shown in fig. S6. The representative FD distributions ($f(\epsilon)$) at three different N_{photon} values are shown in Fig. 4A, and the corresponding electron distributions [calculated as $f(\epsilon)g(\epsilon)$, where $g(\epsilon)$ is graphene density of states] in Fig. 4B. The calculated QY with φ_B of 0.7 eV is shown in Fig. 4C, assuming that all hot electrons above φ_B emit into the semiconductor conduction band with unity yield. As expected, hot electron temperature and injection QY show a strong dependence on both $\hbar\nu$ and N_{photon} . A hotter electron distribution, thus higher QY, can be achieved by increasing either $\hbar\nu$ or N_{photon} , i.e., they are interchangeable. QY reaches ~30% for $\hbar\nu$ of 1.6 eV and N_{photon} of 10^{13} cm⁻². The injected electron density at a fixed $\hbar\nu$ shows a super-linear dependent on N_{photon} or excitation power (fig. S7), consistent with previous photocurrent measurements (26, 28). Simply speaking, as T_e in graphene depends on excitation power (P) as $T_e \sim P^{1/3}$ and thermionic current increases exponentially with T_e , photothermionic current exhibits an overall superlinear dependence (26, 28). Apparently, the high QY value (~50% at 1.6 eV) and especially the linear power

dependence (or constant QY versus N_{photon}) observed experimentally cannot be explained by the conventional 1 μ PTE model.

Instead, the ultrafast electron transfer from photoexcited graphene to the TMD semiconductor suggests that hot electron injection likely occurs before electron-hole coalescence through the 2 μ PTE pathway. In this pathway, on the order of ~10 fs, photoexcited electrons and holes quickly establish separate quasi-thermal equilibrium

$$f_{e(h)}(\epsilon) = \frac{1}{\exp\left(\frac{\epsilon - \mu_{e(h)}^*}{k_B T_{e(h)}^*}\right) + 1} \quad (2)$$

with distinct temperatures ($T_{e(h)}^*$) and separated chemical potentials ($\mu_{e(h)}^*$) for electrons and holes, respectively. Given the ultrafast time scale and phase space constraint of a graphene Dirac spectrum, both photon energy (half into each band) and photoexcited electrons and holes (= N_{photon}) can be approximated to be stored and conserved in each band (16, 18).

We calculated hot electron distribution and injection QY using the proposed 2 μ PTE model. The calculated T_e^* and μ_e^* as a function of $\hbar\nu$ and N_{photon} is shown in fig. S6. The representative FD distributions and corresponding electron distributions above the Dirac point are shown in Fig. 4 (D and E). Obviously, the 2 μ PTE model yields a significantly higher electron temperature and more energetic electrons above φ_B than the 1 μ PTE model, especially at low N_{photon} . For low and moderate N_{photon} (e.g., less than 10^{13} cm⁻²), T_e^* increases linearly with $\hbar\nu$ and μ_e^* is mostly negative (below the Dirac point),

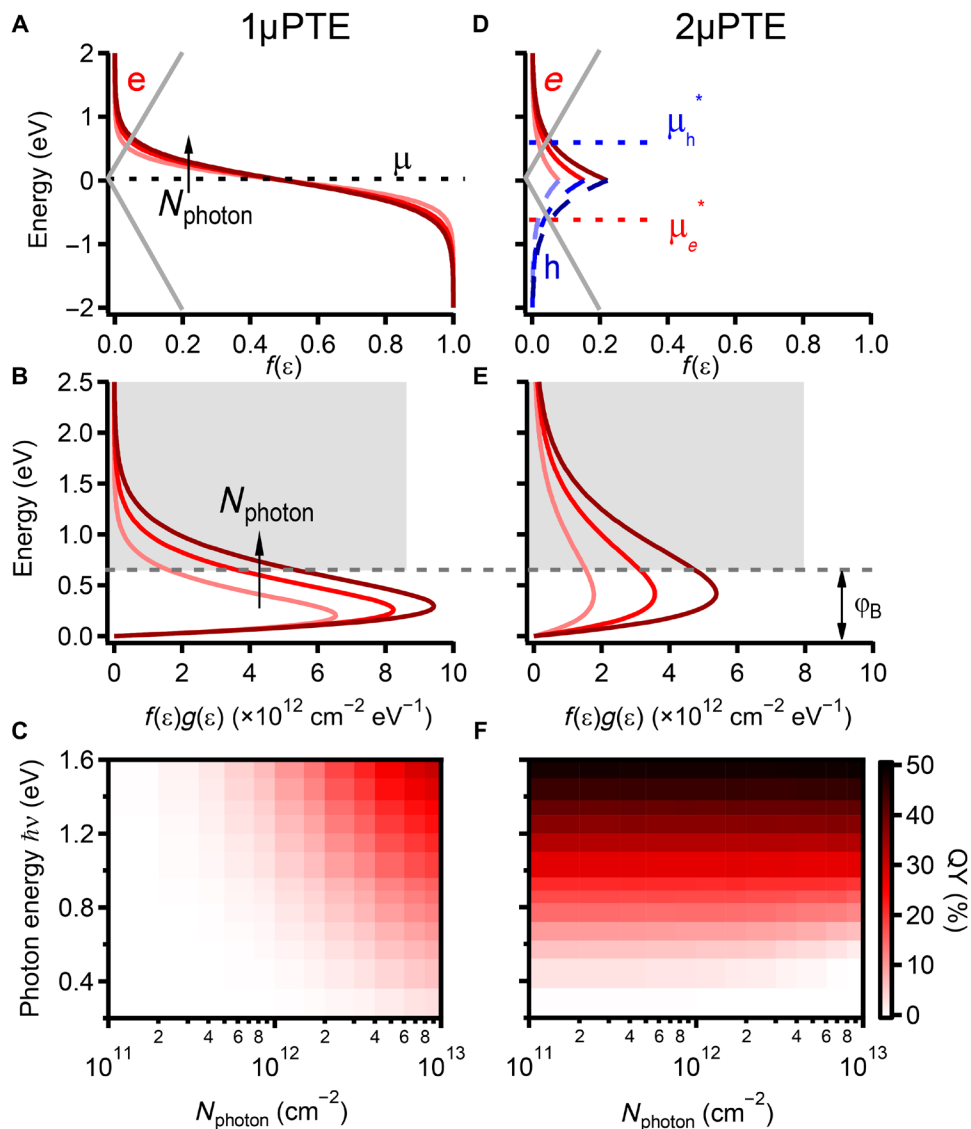


Fig. 4. Comparison between conventional $1\mu\text{PTE}$ model and proposed $2\mu\text{PTE}$ model. (A) 1μ and (D) 2μ models where photoexcitation generates thermalized electrons characterized with one FD distribution in the former but quasi-thermalized electrons and holes with two FD distributions in the latter. Zero denotes the Dirac point. N_{photon} increases as 2×10^{12} , 4×10^{12} , and $6 \times 10^{12} \text{ cm}^{-2}$, and $\hbar\nu$ is fixed at 1.6 eV. Electron distribution above the Dirac point in graphene with (B) 1μ and (E) 2μ models at different absorbed photon densities. Hot electrons above the barrier height (ϕ_B) can inject into the semiconductor conduction band. A much higher fraction of energetic electrons are observed in 2μ model. Color plot of predicted electron injection QY as a function of photon energy and density with (C) $1\mu\text{PTE}$ and (F) $2\mu\text{PTE}$ models. ϕ_B was chosen to be 0.7 eV, and all electrons above ϕ_B were assumed to inject into the semiconductor conduction band. QY shows a strong dependence on both photon energy and density in the $1\mu\text{PTE}$ pathway but remains nearly constant with varying photon density in the $2\mu\text{PTE}$ pathway.

corresponding to a hot and dilute Maxwellian electron gas (Fig. 4D). Therefore, the electron distribution increases almost uniformly (Fig. 4E) with N_{photon} , and the fraction of energetic electrons above ϕ_B (i.e., injection QY) remain nearly constant at fixed $\hbar\nu$ (Fig. 4F and fig. S7). This agrees well with experimentally observed linear power dependence. With further increasing N_{photon} , the classical electron gas gradually transits into a degenerate fermion system where T_e^* goes down and μ_e^* increases to accommodate photoexcited electrons in phase space (fig. S6) (16, 42). Therefore, the fraction of energetic electrons and QY decrease. This is especially obvious for low-energy photon excitations, which explains the onset of sublinear deviation at high N_{photon} ($> 3 \times 10^{13} \text{ cm}^{-2}$) for mid-IR photons.

In Fig. 3D, we show calculated QY versus $\hbar\nu$ with ϕ_B of 0.6 to 0.8 eV and experimental QY values mostly fall into the calculated range. The ϕ_B 0.2 to 0.3 eV smaller than values from quasi-particle band alignment can be attributed to interlayer exciton binding energy, which is 0.2 to 0.3 eV in two-dimensional layered heterostructures (36, 37, 43). Considering no free parameters, this simple $2\mu\text{PTE}$ model reproduced the experimental results reasonably well and captured the key essence: the highly efficient harnessing of energetic electron from intraband scattering, prevailing over energy and carrier loss due to interband scattering and phonon emission.

To further support the proposed $2\mu\text{PTE}$ pathway, we measured the hot electron injection yield as a function of sample temperature

(Fig. 3E) and back gate voltage (V_G) (Fig. 3F). In contrast to graphene hot carrier devices based on the thermoelectric effect (22–24), we observed no clear temperature effect, confirming that the absence of acoustic phonon involved cooling loss in the hot carrier extraction process. Applying back gate voltage alters carrier doping type and concentration in graphene. Since graphene in the heterostructure is slightly p-doped with chemical potential near the Dirac point, a negative (positive) V_G dopes holes (electrons) in graphene. As shown in Fig. 3F, the hot electron injection yield shows negligible dependence on hole doping but a continuous decrease with increasing electron doping concentration, confirming hot electron transfer after intraband electron scattering before electron-hole interband coalescence.

We extended this hot electron-assisted photocarrier generation under sub-bandgap excitation to other TMD semiconductors including MoS₂, MoSe₂, and WSe₂, indicating the general applicability of this broadband energy-harvesting strategy (figs. S8 and S12). A thorough study on a Gr/WSe₂ heterostructure with $\hbar\nu$ and N_{photon} yields a similar linear power dependence and a strongly increasing QY with $\hbar\nu$ (section S6). The results can also be described by the $2\mu\text{PTE}$ model with ϕ_B of 0.8 to 1.0 eV, which is consistent with the higher CBM of WSe₂ (44). Achieving $2\mu\text{PTE}$ regime requires ultrafast electron intraband scattering coupled with an equally fast interfacial electron transfer before electron-phonon/hole scattering. Van der Waals stacking between atomically flat high-quality graphene and a layered semiconductor to form ultimate contact seems to be the key here. Coupling graphene to other systems, e.g., Si, GaAs bulk semiconductors to achieve $2\mu\text{PTE}$ would be highly interesting but requires careful interface control.

DISCUSSION

Compared to conventional pathways, $2\mu\text{PTE}$ proposed here yields significantly higher hot electron extraction QY especially at a technically relevant low-fluence regime, e.g., solar radiation. The highly efficient hot carrier generation and extraction from graphene over a broad spectral range through the $2\mu\text{PTE}$ pathway closely resembles the concept of “hot carrier solar cell” introduced in the beginning. This, together with facial van der Waals stacking without lattice constraint, sets graphene apart from conventional semiconductor systems and points to a new route for extremely efficient and flexible energy-harvesting and optoelectronic devices beyond the standard limit. Furthermore, the efficient generation and harnessing of energetic electrons above (~1 eV) the Dirac point with low-energy photons also suggest graphene as potential broadband upconverting light-harvesting component to drive chemical reactions (e.g., photocatalysis). The absorption can be increased using optical waveguides and/or plasmon enhancement. The fast back electron transfer to graphene (i.e., charge recombination loss) can be retarded by constructing judiciously designed multicomponent vertical heterostructures (e.g., Gr/WS₂/MoS₂; see section S2).

MATERIALS AND METHODS

Sample preparation

Isolated graphene and TMD layers were mechanically exfoliated onto transparent SiO₂ or SiO₂ (100 nm)/Si substrates from bulk crystals (HQ graphene). The number of layers was confirmed by atomic force microscopy, PL, and Raman spectroscopy. After the TMD and graphene monolayers were exfoliated onto the substrates, we picked up the

graphene monolayer with polycarbonate (PC) and transferred on top of a TMD flake under an optical microscope to form a Gr/TMD heterostructure. The PC was melted at 180°C and dissolved with chloroform. The samples were annealed for 1 hour at 300°C in high vacuum.

Optical characterization

Steady-state micro-area PL, Raman, transmittance, and reflectance contrast measurements were taken on a home-built microscope setup. A supercontinuum laser (NKT, super compact) was used as broadband light source for transmittance and reflectance contrast measurement and a 532-nm continuous-wave laser (full width at half maximum, <0.001 nm) for PL and Raman measurements. Spectra were recorded with a liquid N₂ cooled detector (Princeton Instruments). For femtosecond TR spectroscopy (mFemto-TR100, Time-Tech Spectra LLC) (39), the fundamental output (1030 nm, ~170-fs pulse duration) from a Yb:KGW laser (PHAROS, Light Conversion Ltd.) was separated into multiple light beams. One was introduced to a noncollinear optical parametric amplifier (OPA) to generate visible and near-IR wavelengths for pump beam (775, 900, 1300, 1500, 1700, and 2000 nm, with a pulse duration of 30 to 100 fs depending on the wavelength), and one was introduced to a collinear OPA to generate 2.4 and 3.5 μm with a pulse duration of ~170 fs. The third was focused onto an yttrium-aluminum-garnet crystal to generate continuum white light as a probe beam. Both pump and probe beams were sent to a microscope colinearly and focused using a reflective microscope on the sample. The exact beam profile for both the pump and the probe can be seen in fig. S5. Samples were in a liquid nitrogen-cooled cryostat for low-temperature TR measurements. Back gate voltage was applied with prepatterned electrodes and KEITHLEY 2614B.

SUPPLEMENTARY MATERIALS

Supplementary material for this article is available at <http://advances.sciencemag.org/cgi/content/full/5/11/eaax9958/DC1>

- Section S1. Determining doping level and chemical potential in graphene
- Section S2. Selective carrier extraction from Gr/WS₂ heterostructures and charge recombination retardation
- Section S3. QY calibration using WSe₂/WS₂ heterostructure and direct high-energy excitation
- Section S4. Absorbed photon density calculation
- Section S5. Calculation with $1\mu\text{PTE}$ model and $2\mu\text{PTE}$ model
- Section S6. Hot electron transfer from photoexcited graphene to WSe₂
- Section S7. Additional figures
- Fig. S1. Determining doping level and chemical potential in graphene.
- Fig. S2. Selective carrier extraction and charge recombination retardation.
- Fig. S3. CT in WSe₂/WS₂ heterostructure.
- Fig. S4. TR measurements of Gr/WS₂ under above-gap excitation.
- Fig. S5. Beam profile and absorption properties of heterostructures.
- Fig. S6. Calculated carrier temperature and chemical potential with different models.
- Fig. S7. Calculated injection electron density.
- Fig. S8. Hot electron transfer from photoexcited graphene to WSe₂.
- Fig. S9. PL spectra of WS₂ monolayer and Gr/WS₂ heterostructure.
- Fig. S10. All TR kinetics of Gr/WS₂ heterostructure at WS₂ A exciton bleach, at different excitation photon energies and densities.
- Fig. S11. TR results from another Gr/WS₂ sample.
- Fig. S12. TR spectra of Gr/MoS₂ and Gr/MoSe₂ heterostructures.
- References (45–48)

REFERENCES AND NOTES

1. W. Shockley, H. J. Queisser, Detailed balance limit of efficiency of p-n junction solar cells. *J. Appl. Phys.* **32**, 510–519 (1961).
2. R. T. Ross, A. J. Nozik, Efficiency of hot-carrier solar energy converters. *J. Appl. Phys.* **53**, 3813–3818 (1982).
3. W. A. Tisdale, K. J. Williams, B. A. Timp, D. J. Norris, E. S. Aydil, X.-Y. Zhu, Hot-electron transfer from semiconductor nanocrystals. *Science* **328**, 1543–1547 (2010).
4. M. L. Brongersma, N. J. Halas, P. Nordlander, Plasmon-induced hot carrier science and technology. *Nat. Nanotechnol.* **10**, 25–34 (2015).

5. J. C. Song, L. S. Levitov, Energy flows in graphene: Hot carrier dynamics and cooling. *J. Phys. Condens. Matter* **27**, 164201 (2015).
6. K. F. Mak, M. Y. Sfeir, Y. Wu, C. H. Lui, J. A. Misewich, T. F. Heinz, Measurement of the optical conductivity of graphene. *Phys. Rev. Lett.* **101**, 196405 (2008).
7. R. R. Nair, P. Blake, A. N. Grigorenko, K. S. Novoselov, T. J. Booth, T. Stauber, N. M. R. Peres, A. K. Geim, Fine structure constant defines visual transparency of graphene. *Science* **320**, 1308 (2008).
8. M. Breusing, S. Kuehn, T. Winzer, E. Malic, F. Milde, N. Severin, J. P. Rabe, C. Ropers, A. Knorr, T. Elsaesser, Ultrafast nonequilibrium carrier dynamics in a single graphene layer. *Phys. Rev. B* **83**, 153410 (2011).
9. D. Brida, A. Tomadin, C. Manzoni, Y. J. Kim, A. Lombardo, S. Milana, R. R. Nair, K. S. Novoselov, A. C. Ferrari, G. Cerullo, M. Polini, Ultrafast collinear scattering and carrier multiplication in graphene. *Nat. Commun.* **4**, 1987 (2013).
10. A. Tomadin, D. Brida, G. Cerullo, A. C. Ferrari, M. Polini, Nonequilibrium dynamics of photoexcited electrons in graphene: Collinear scattering, Auger processes, and the impact of screening. *Phys. Rev. B* **88**, 035430 (2013).
11. S. Gilbertson, G. L. Dakovski, T. Durakiewicz, J.-X. Zhu, K. M. Dani, A. D. Mohite, A. Dattelbaum, G. Rodriguez, Tracing ultrafast separation and coalescence of carrier distributions in graphene with time-resolved photoemission. *J. Phys. Chem. Lett.* **3**, 64–68 (2012).
12. I. Gierz, J. C. Petersen, M. Mitrano, C. Cacho, I. C. Turcu, E. Springate, A. Stöhr, A. Köhler, U. Starke, A. Cavalleri, Snapshots of non-equilibrium Dirac carrier distributions in graphene. *Nat. Mater.* **12**, 1119–1124 (2013).
13. M. Breusing, C. Ropers, T. Elsaesser, Ultrafast carrier dynamics in graphite. *Phys. Rev. Lett.* **102**, 086809 (2009).
14. W.-T. Liu, S. W. Wu, P. J. Schuck, M. Salmeron, Y. R. Shen, F. Wang, Nonlinear broadband photoluminescence of graphene induced by femtosecond laser irradiation. *Phys. Rev. B* **82**, 081408 (2010).
15. C. H. Lui, K. F. Mak, J. Shan, T. F. Heinz, Ultrafast photoluminescence from graphene. *Phys. Rev. Lett.* **105**, 127404 (2010).
16. T. Li, L. Luo, M. Hupalo, J. Zhang, M. C. Tringides, J. Schmalian, J. Wang, Femtosecond population inversion and stimulated emission of dense dirac fermions in graphene. *Phys. Rev. Lett.* **108**, 167401 (2012).
17. I. Gierz, M. Mitrano, J. C. Petersen, C. Cacho, I. C. Edmond Turcu, E. Springate, A. Stöhr, A. Köhler, U. Starke, A. Cavalleri, Population inversion in monolayer and bilayer graphene. *J. Phys. Condens. Matter* **27**, 164204 (2015).
18. E. Malic, T. Winzer, E. Bobkin, A. Knorr, Microscopic theory of absorption and ultrafast many-particle kinetics in graphene. *Phys. Rev. B* **84**, 205406 (2011).
19. X. Xu, N. M. Gabor, J. S. Alden, A. M. van der Zande, P. L. McEuen, Photo-thermoelectric effect at a graphene interface junction. *Nano Lett.* **10**, 562–566 (2010).
20. N. M. Gabor, J. C. W. Song, Q. Ma, N. L. Nair, T. Taychatanapat, K. Watanabe, T. Taniguchi, L. S. Levitov, P. Jarillo-Herrero, Hot carrier-assisted intrinsic photoresponse in graphene. *Science* **334**, 648–652 (2011).
21. S. Wu, L. Wang, Y. Lai, W.-Y. Shan, G. Avizian, X. Zhang, T. Taniguchi, K. Watanabe, D. Xiao, C. Dean, J. Hone, Z. Li, X. Xu, Multiple hot-carrier collection in photo-excited graphene Moiré superlattices. *Sci. Adv.* **2**, e1600002 (2016).
22. K. J. Tielrooij, L. Piatkowski, M. Massicotte, A. Woessner, Q. Ma, Y. Lee, K. S. Myhro, C. N. Lau, P. Jarillo-Herrero, N. F. van Hulst, F. H. Koppens, Generation of photovoltage in graphene on a femtosecond timescale through efficient carrier heating. *Nat. Nanotechnol.* **10**, 437–443 (2015).
23. M. W. Graham, S.-F. Shi, D. C. Ralph, J. Park, P. L. McEuen, Photocurrent measurements of supercollision cooling in graphene. *Nat. Phys.* **9**, 103–108 (2013).
24. D. Sun, G. Avizian, A. M. Jones, J. S. Ross, W. Yao, D. Cobden, X. Xu, Ultrafast hot-carrier-dominated photocurrent in graphene. *Nat. Nanotechnol.* **7**, 114–118 (2012).
25. M. Long, E. Liu, P. Wang, A. Gao, H. Xia, W. Luo, B. Wang, J. Zeng, Y. Fu, K. Xu, W. Zhou, Y. Lv, S. Yao, M. Lu, Y. Chen, Z. Ni, Y. You, X. Zhang, S. Qin, Y. Shi, W. Hu, D. Xing, F. Miao, Broadband photovoltaic detectors based on an atomically thin heterostructure. *Nano Lett.* **16**, 2254–2259 (2016).
26. M. Massicotte, P. Schmidt, F. Vialla, K. Watanabe, T. Taniguchi, K. J. Tielrooij, F. H. L. Koppens, Photo-thermionic effect in vertical graphene heterostructures. *Nat. Commun.* **7**, 12174 (2016).
27. L. Yuan, T.-F. Chung, A. Kuc, Y. Wan, Y. Xu, Y. P. Chen, T. Heine, L. B. Huang, Photocurrent generation from interlayer charge-transfer transitions in WS₂-graphene heterostructures. *Sci. Adv.* **4**, e1700324 (2018).
28. Q. Ma, T. I. Andersen, N. L. Nair, N. M. Gabor, M. Massicotte, H. C. Lui, A. F. Young, W. Fang, K. Watanabe, T. Taniguchi, J. Kong, N. Gedik, F. H. L. Koppens, P. Jarillo-Herrero, Tuning ultrafast electron thermalization pathways in a van der Waals heterostructure. *Nat. Phys.* **12**, 455–459 (2016).
29. R. Urcuyo, D. L. Duong, P. Sailer, M. Burghard, K. Kern, Hot carrier extraction from multilayer graphene. *Nano Lett.* **16**, 6761–6766 (2016).
30. M. Trushin, Theory of photoexcited and thermionic emission across a two-dimensional graphene-semiconductor Schottky junction. *Phys. Rev. B* **97**, 195447 (2018).
31. J. F. Rodriguez-Nieva, M. S. Dresselhaus, J. C. W. Song, Enhanced thermionic-dominated photoresponse in graphene schottky junctions. *Nano Lett.* **16**, 6036–6041 (2016).
32. G. Froehlicher, E. Lorchat, S. Berciaud, Charge versus energy transfer in atomically thin graphene-transition metal dichalcogenide van der Waals heterostructures. *Phys. Rev. X* **8**, 011007 (2018).
33. H. Henck, Z. Ben Aziza, D. Pierucci, F. Laourine, F. Reale, P. Palczynski, J. Chaste, M. G. Silly, F. Bertran, P. Le Fèvre, E. Lhuillier, T. Wakamura, C. Mattevi, J. E. Rault, M. Calandra, A. Ouerghi, Electronic band structure of two-dimensional WS₂/graphene van der Waals heterostructures. *Phys. Rev. B* **97**, 155421 (2018).
34. A. Chernikov, T. C. Berkelbach, H. M. Hill, A. Rigosi, Y. Li, O. B. Aslan, D. R. Reichman, M. S. Hybertsen, T. F. Heinz, Exciton binding energy and nonhydrogenic rydberg series in monolayer WS₂. *Phys. Rev. Lett.* **113**, 076802 (2014).
35. A. Raja, A. Chaves, J. Yu, G. Arefe, H. M. Hill, A. F. Rigosi, T. C. Berkelbach, P. Nagler, C. Schüller, T. Korn, C. Nuckolls, J. Hone, L. E. Brus, T. F. Heinz, D. R. Reichman, A. Chernikov, Coulomb engineering of the bandgap and excitons in two-dimensional materials. *Nat. Commun.* **8**, 15251 (2017).
36. X. Wen, H. Chen, T. Wu, Z. Yu, Q. Yang, J. Deng, Z. Liu, X. Guo, J. Guan, X. Zhang, Y. Gong, J. Yuan, Z. Zhang, C. Yi, X. Guo, P. M. Ajayan, W. Zhuang, Z. Liu, J. Lou, J. Zheng, Ultrafast probes of electron-hole transitions between two atomic layers. *Nat. Commun.* **9**, 1859 (2018).
37. X. Zhu, N. R. Monahan, Z. Gong, H. Zhu, K. W. Williams, C. A. Nelson, Charge transfer excitons at van der Waals interfaces. *J. Am. Chem. Soc.* **137**, 8313–8320 (2015).
38. H. M. Hill, A. F. Rigosi, A. Raja, A. Chernikov, C. Roquelet, T. F. Heinz, Exciton broadening in WS₂/graphene heterostructures. *Phys. Rev. B* **96**, 205401 (2017).
39. H. Zhou, Y. Zhao, H. Zhu, Dielectric environment-robust ultrafast charge transfer between two atomic layers. *J. Phys. Chem. Lett.* **10**, 150–155 (2019).
40. J. He, N. Kumar, M. Z. Bellus, H.-Y. Chiu, D. He, Y. Wang, H. Zhao, Electron transfer and coupling in graphene-tungsten disulfide van der Waals heterostructures. *Nat. Commun.* **5**, 5622 (2014).
41. K. J. Tielrooij, J. C. W. Song, S. A. Jensen, A. Centeno, A. Pesquera, A. Zurutuza Elorza, M. Bonn, L. S. Levitov, F. H. L. Koppens, Photoexcitation cascade and multiple hot-carrier generation in graphene. *Nat. Phys.* **9**, 248–252 (2013).
42. J. Zhang, J. Schmalian, T. Li, J. Wang, Transient charge and energy balance in graphene induced by ultrafast photoexcitation. *J. Phys. Condens. Matter* **25**, 314201 (2013).
43. N. R. Wilson, P. V. Nguyen, K. Seyler, P. Rivera, A. J. Marsden, Z. P. L. Laker, G. C. Constantinescu, V. Kandyba, A. Barinov, N. D. M. Hine, X. Xu, D. H. Cobden, Determination of band offsets, hybridization, and exciton binding in 2D semiconductor heterostructures. *Sci. Adv.* **3**, e1601832 (2017).
44. J. Kang, S. Tongay, J. Zhou, J. B. Li, J. Q. Wu, Band offsets and heterostructures of two-dimensional semiconductors. *Appl. Phys. Lett.* **102**, 012111 (2013).
45. S. Pisana, M. Lazzeri, C. Casiraghi, K. S. Novoselov, A. K. Geim, A. C. Ferrari, F. Mauri, Breakdown of the adiabatic Born–Oppenheimer approximation in graphene. *Nat. Mater.* **6**, 198–201 (2007).
46. A. Das, S. Pisana, B. Chakraborty, S. Piscanec, S. K. Saha, U. V. Waghmare, K. S. Novoselov, H. R. Krishnamurthy, A. K. Geim, A. C. Ferrari, A. K. Sood, Monitoring dopants by Raman scattering in an electrochemically top-gated graphene transistor. *Nat. Nanotechnol.* **3**, 210–215 (2008).
47. K. Wang, B. Huang, M. Tian, F. Ceballos, M. W. Lin, M. Mahjouri-Samani, A. Boulesbaa, A. A. Puzosky, C. M. Rouleau, M. Yoon, H. Zhao, K. Xiao, G. Duscher, D. B. Geohegan, Interlayer coupling in twisted wse₂/ws₂ bilayer heterostructures revealed by optical spectroscopy. *ACS Nano* **10**, 6612–6622 (2016).
48. X. Hong, J. Kim, S. F. Shi, Y. Zhang, C. Jin, Y. Sun, S. Tongay, J. Wu, Y. Zhang, F. Wang, Ultrafast charge transfer in atomically thin MoS₂/WS₂ heterostructures. *Nat. Nanotechnol.* **9**, 682–686 (2014).

Acknowledgments

Funding: We thank the National Natural Science Foundation of China (21773208) and National Key Research and Development Program of China (2017YFA0207700) for financial support. **Author contributions:** H. Zhu conceived the study; Y.C. fabricated heterostructure samples with help from Y.L. and H. Zhou; Y.C. and Y.L. performed the optical measurements. Y.Z. performed the modeling. H. Zhu wrote the manuscript. All authors revised the manuscript. **Competing interests:** The authors declare that they have no competing interests. **Data and materials availability:** All data needed to evaluate the conclusions in the paper are present in the paper and/or the Supplementary Materials. Additional data related to this paper may be requested from the authors.

Submitted 10 May 2019
 Accepted 7 October 2019
 Published 29 November 2019
 10.1126/sciadv.aax9958

Citation: Y. Chen, Y. Li, Y. Zhao, H. Zhou, H. Zhu, Highly efficient hot electron harvesting from graphene before electron-hole thermalization. *Sci. Adv.* **5**, eaax9958 (2019).